[redacted] Stochastic Gravitational Wave Background from Non-Tensorial Polarizations

Sylvia Biscoveanu and Thomas Callister
California Institute of Technology
LIGO SURF Program
DCC T1600155

September 22, 2016

Abstract

The first direct detection of gravitational waves was recently announced by the LIGO (Laser Interferometer Gravitational Wave Observatory) Collaboration. Besides the chirp waves produced by compact binary coalescences as in the case of the first event, a stochastic gravitational wave background is expected to arise due to the overlap of many individually indistinguishable sources that are both astrophysical and cosmological in nature. General Relativity predicts two tensorial gravitational wave polarization modes, but general metric theories of gravity allow four additional scalar and vector modes. Detection of these non-tensorial polarizations in the stochastic background would indicate that the theory of gravity should be extended beyond General Relativity. While the unique separation of the three types of polarizations is not possible given a two-detector network like LIGO, we compute the signal-to-noise ratio assuming a stochastic background dominated by each mode [redacted]

1 Introduction

1.1 The Stochastic Background

A random gravitational wave background is predicted as a result of many overlapping, individually indistinguishable sources, which may be both astrophysical and cosmological in nature. Such sources include compact binary coalescences, core collapse supernovae, inflation, phase transitions, and cosmic strings, among others [1]. A background dominated by astrophysical sources would provide information on the star formation history, merger rates of compact binaries, and the mass range of the progenitor systems. Meanwhile the detection of a cosmological background would offer insight into the state of the universe in the moments immediately following the Big Bang [2].

When conducting searches for the stochastic background, one typically seeks to measure the ratio of the energy contribution due to gravitational waves to the critical energy density, $\rho_c = \frac{3c^2 H_0^2}{8\pi G}$, needed to close the Universe:

$$\Omega_{gw} = \frac{1}{\rho_c} \frac{d\rho_{gw}}{d \ln f} \tag{1}$$

where H_0 is the Hubble expansion rate [1]. The gravitational wave energy density describes the spectrum of the stochastic background as a function of frequency and is often modeled as a power law,

$$\Omega_{gw} = \Omega_{\alpha}(f/f_0)^{\alpha}, \tag{2}$$

where $\alpha = 2/3$ for astrophysical backgrounds and $\alpha = 0$ for cosmological sources and f_0 is an arbitrary reference frequency [3]. The current best upper limit on the stochastic gravitational wave background energy density from the ground-based LIGO and Virgo detectors is $\Omega_{gw} < 5.6 \times 10^{-6}$ [4].

Certain statistical assumptions must be made to give a more robust description of the stochastic background than that provided by the spectrum alone. We assume that such a background is stationary, isotropic, unpolarized, and Gaussian. For a signal to be stationary, it must depend only on the differences between observation times and not on the absolute times themselves. Because the age of the Universe is at least 20 orders of magnitude larger than the period of gravitational waves detected by ground–based interferometers, no time dependence is anticipated [1].

If the stochastic background is analogous to the Cosmic Microwave Background, it is justified to assume that it would be highly isotropic. However, the directional dependence of the background will ultimately depend on its sources. For example, a stochastic background dominated by coalescing binaries in one area of the sky will be highly anisotropic, while one resulting largely from cosmological sources will show no directional dependence.

The final assumption is proven by the Central Limit Theorem, which states that any random process created by the superposition of independent random variables will be Gaussian [5]. As long as the stochastic background is a result of many overlapping and independent gravitational wave signals whose individual duration is much larger than the time between events, its statistical properties will be entirely determined by the first and second moments of the strain recorded in a detector [2]. However, the Gaussianity of the signal is also source-dependent. A black hole background, for example, is expected to be populated by events whose duration is shorter than the time separating them, which would result in a non-Gaussian, 'popcorn' signal where waveforms no longer overlap and the amplitude at the detector is unpredictable at a given time [2].

1.2 Gravitational Wave Polarizations

In General Relativity, gravitational waves are transverse, represented by second-rank, symmetric, traceless tensors [6]. This theory only allows two states of polarization–the plus and the cross modes–but in a general metric theory of gravity up to six independent polarizations are allowed. Besides the two tensor modes allowed by GR, these include the x and y vector modes and the longitudinal and breathing scalar modes with basis tensors given by

$$\tilde{e}^{+}_{ij} = \begin{pmatrix} 1 & 0 & 0 \\ 0 & -1 & 0 \\ 0 & 0 & 0 \end{pmatrix}, \quad \tilde{e}^{\times}_{ij} = \begin{pmatrix} 0 & 1 & 0 \\ 1 & 0 & 0 \\ 0 & 0 & 0 \end{pmatrix},$$

$$\tilde{e}^{x}_{ij} = \begin{pmatrix} 0 & 0 & 1 \\ 0 & 0 & 0 \\ 1 & 0 & 0 \end{pmatrix}, \quad \tilde{e}^{y}_{ij} = \begin{pmatrix} 0 & 0 & 0 \\ 0 & 0 & 1 \\ 0 & 1 & 0 \end{pmatrix},$$

$$\tilde{e}^{l}_{ij} = \sqrt{2}\begin{pmatrix} 0 & 0 & 0 \\ 0 & 0 & 0 \\ 0 & 0 & 1 \end{pmatrix}, \quad \tilde{e}^{b}_{ij} = \begin{pmatrix} 1 & 0 & 0 \\ 0 & 1 & 0 \\ 0 & 0 & 0 \end{pmatrix},$$

for a GW propagating in the z direction [7]. The tildes denote that the definitions are given in 3-dimensional Euclidean space rather than in 4-dimensional Minkowski spacetime. Unlike the plus and cross modes of General Relativity, the scalar modes are not traceless. The effect of each type of polarization on a test mass ring is shown in Figure 1.

Depending on the corresponding gravity theory, these extra polarizations are due to the extra degrees of freedom associated with scalar fields or to the ability of the graviton to propagate into extra dimensions. Not all modes appear in all theoretical models; most of the cosmologically interesting theories are of the scalar-tensor variant, in which no vector polarization appears [7]. While a tensor stochastic background has not yet been detected, a search for these additional non-tensorial polarizations would test the limits of GR. If extra polarizations were detected, this would indicate that the theory of gravitation should be extended beyond General Relativity, while a nondetection could exclude certain theoretical models. Besides the implications for gravitational theory, GW polarizations can also provide information about the orientation of their progenitor systems and about the accelerated expansion of the universe [6] [7].

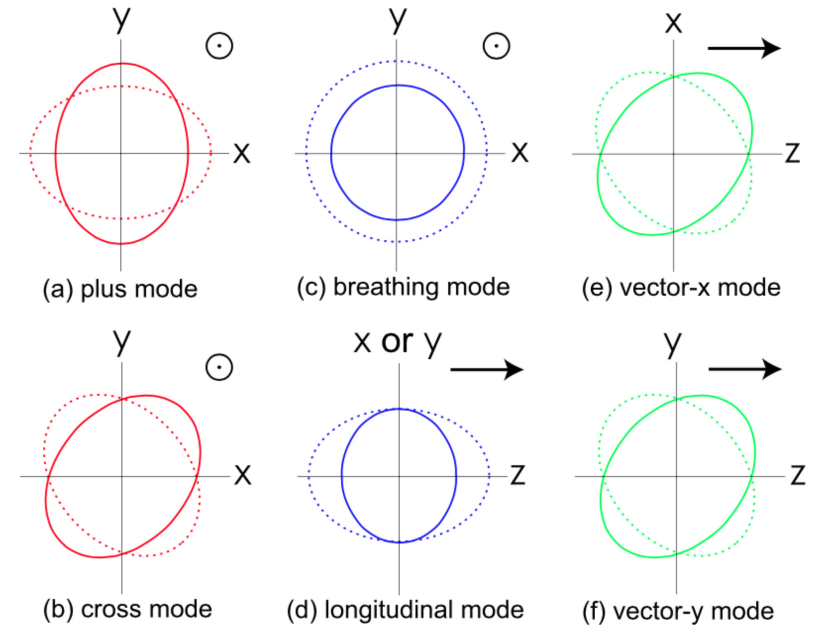

Figure 1: Graphic from [7] showing the effect of a passing gravitational wave with each polarization on a test mass ring, with the direction of propagation given in the upper right corer. The $\odot$ symbol indicates that the wave vector is directed into the page.

This analysis seeks to extend the current stochastic search framework to non-tensorial polarizations. The modifications to the stochastic pipeline will be tested on simulated noise and ultimately on both singly-polarized and mixed-polarization simulated signal. The modified pipeline will be used to conduct the search for alternative polarizations in aLIGO data [redacted]. We also develop a model selection procedure with which to separate the amplitudes due to each polarization for a signal of a fixed spectral shape in a two-detector pair.

1.3 The LIGO Detector

In order to detect a stochastic background, the strain data from two detectors must be cross–correlated. In a single detector, the noise would be much louder than the astrophysical contribution from a stochastic background. By cross–correlating the total strain, this effectively mitigates uncorrelated noise, and the resulting signal is dominated by the astrophysical contribution. The Laser Interferometer Gravitational Wave Observatory (LIGO) is a pair of ground based interferometers located in Hanford, Washington, and Livingston, Louisiana. Each detector consists of a Michelson Interferometer with 4 km long arms, with a Fabry–Pérot cavity in each arm. Laser light is sent to a beam splitter, which in turn redirects the beam to travel down the two arms. Upon reaching the end optics, the light is reflected and recombined at the beam splitter and sent to a photodetector. The effect of a gravitational wave is to compress the arm length in one direction while stretching it in the perpendicular direction. This results in a phase shift between the two light beams, producing an interference pattern that is recorded by the photodetector upon recombination [8].

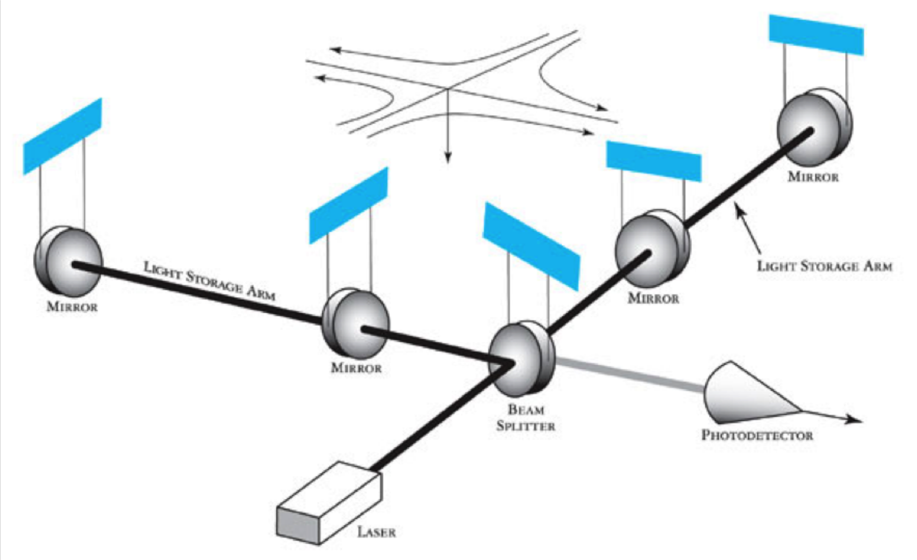

Figure 2: Schematic of a Michelson Interferometer from [9] like the one used in the two LIGO observatories. Laser light incident on the beam splitter is sent down the two arms and reflected back by the end test mass. In the presence of a gravitational wave, the arm length will be compressed in one direction and extended in the other, leading to a phase shift observable as an interference pattern in the recombined light received by the photodetector.

After a series of updates to the Initial LIGO instrument, the Advanced LIGO (aLIGO) detector completed its first science run in January 2016. The laser power was increased from 10 W to 20 W, with a corresponding increase in both the diameter and the mass of the end mirrors. Initial LIGO used 25 cm, 11 kg fused silica masses, while those used in aLIGO are 34 cm with a mass of 40 kg. The diameter increase will counteract thermal noise and the increase in mass minimizes the effects of shot noise. The suspension system has also been upgraded to a four–pendulum setup, with fused silica fibers replacing the previously used steel wires. This upgrade to the seismic isolation system has extended the lower limit of the frequency band from 40 Hz down to 20 Hz [10].

The combined effect of the system upgrades will be to improve the sensitivity across the entire frequency spectrum by at least a factor of 10 and to deepen the field of view of the detector. For example, binary systems made up of $1.4\mathrm{M}_\odot$ inspiraling neutron stars will be detectable at distances 15 times greater than with Initial LIGO [10]. A coalescing binary black hole system was detected by the aLIGO instrument on September 14th, 2015, representing the first direct detection of gravitational waves. A second BBH event was observed on December 26th, 2015, and along with another candidate event (which didn't pass the detection procedure due to a much higher false alarm rate) ushered in the era of gravitational wave astronomy [11].

2 Formalism

2.1 Antenna Pattern Functions

Before beginning the cross-correlated analysis, we consider the response of a single detector to a gravitational wave propagating in the direction of the unit vector $\hat{\mathbf{\Omega}}$. The response function (also called the antenna pattern) of the detector for a specified polarization is given by a tensor contraction between the detector tensor, $\mathbf{D}$, and each polarization tensor $\tilde{\mathbf{e}}_A$, where A denotes each polarization mode [7]:

$$F_A(\hat{\mathbf{\Omega}}) = \mathbf{D} : \tilde{\mathbf{e}}_A(\hat{\mathbf{\Omega}}), \tag{3}$$

$$\mathbf{D} = \frac{1}{2}(\hat{\mathbf{u}} \otimes \hat{\mathbf{u}} - \hat{\mathbf{v}} \otimes \hat{\mathbf{v}}). \tag{4}$$

The unit vectors $\hat{\mathbf{u}}$ and $\hat{\mathbf{v}}$ point along the direction of each of the arms of the interferometer in the Earth-based frame. We define the orthonormal coordinate system of the gravitational wave as:

$$\hat{\mathbf{\Omega}} = (\sin\theta\cos\phi, \sin\theta\sin\phi, \cos\theta), \tag{5}$$

$$\hat{\mathbf{m}} = (\sin\phi, -\cos\phi, 0), \tag{6}$$

$$\hat{\mathbf{n}} = (\cos\phi\cos\theta, \sin\phi\cos\theta, -\sin\theta). \tag{7}$$

In this new frame, the polarization tensors can be written as:

$$\tilde{\mathbf{e}}_+ = \hat{\mathbf{m}} \otimes \hat{\mathbf{m}} - \hat{\mathbf{n}} \otimes \hat{\mathbf{n}}, \qquad \tilde{\mathbf{e}}_\times = \hat{\mathbf{m}} \otimes \hat{\mathbf{n}} + \hat{\mathbf{n}} \otimes \hat{\mathbf{m}}, \tag{8}$$

$$\tilde{\mathbf{e}}_x = \hat{\mathbf{m}} \otimes \hat{\mathbf{\Omega}} - \hat{\mathbf{\Omega}} \otimes \hat{\mathbf{m}}, \qquad \tilde{\mathbf{e}}_y = \hat{\mathbf{n}} \otimes \hat{\mathbf{\Omega}} - \hat{\mathbf{\Omega}} \otimes \hat{\mathbf{n}}, \tag{9}$$

$$\tilde{\mathbf{e}}_b = \hat{\mathbf{m}} \otimes \hat{\mathbf{m}} + \hat{\mathbf{n}} \otimes \hat{\mathbf{n}}, \qquad \tilde{\mathbf{e}}_l = \sqrt{2}\hat{\mathbf{\Omega}} \otimes \hat{\mathbf{\Omega}}. \tag{10}$$

$F_A(\hat{\mathbf{\Omega}})$ is plotted in Figure 4 for all six polarizations. Because the antenna pattern functions for the two scalar modes are degenerate, they cannot be separated by a ground based gravitational wave detector [7].

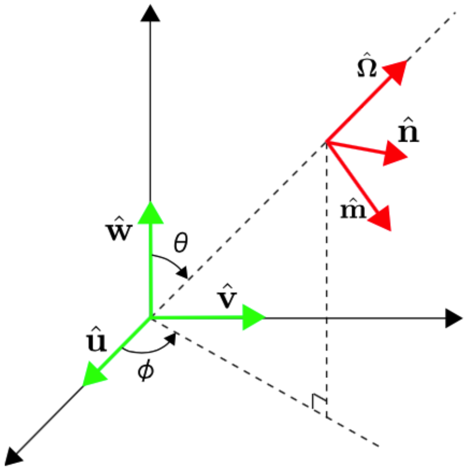

Figure 3: Coordinate systems schematic from [7].

2.2 Cross-Correlation Analysis

The total strain, s in each detector can be written in the Fourier domain as

$$\tilde{s}(f) = \tilde{h}(f) + \tilde{n}(f), \tag{11}$$

where h is the astrophysical contribution and n represents a noise term. At a given position $\vec{\mathbf{X}}$, $\tilde{h}(f)$ can be written as a sum of the contributions from each sky position $\hat{\boldsymbol{\Omega}}$ and wave polarization A,

$$\tilde{h}(f) = \sum_A \int_{S^2} d\hat{\boldsymbol{\Omega}}\, \tilde{h}_A(f, \hat{\boldsymbol{\Omega}}) e^{-2\pi i f \hat{\boldsymbol{\Omega}} \cdot \vec{\mathbf{X}}/c} F_A(f, \hat{\boldsymbol{\Omega}}). \tag{12}$$

The stochastic search seeks to measure the gravitational wave power spectral density, which for a specific polarization is given by

$$S_A(f) \equiv k\langle \tilde{h}^*_A(f) \tilde{h}_A(f) \rangle, \tag{13}$$

where k is the Fourier normalization constant [7]. This quantity is related to the gravitational wave energy density via

$$\Omega_{gw}(f) = \frac{2\pi^2}{3H_0^2} f^3 S_A(f). \tag{14}$$

Assuming the noise is uncorrelated between the two interferometers, the total strain $\tilde{s}(f)$ can be substituted for $\tilde{h}(f)$ in the power spectral density without any loss of generality.

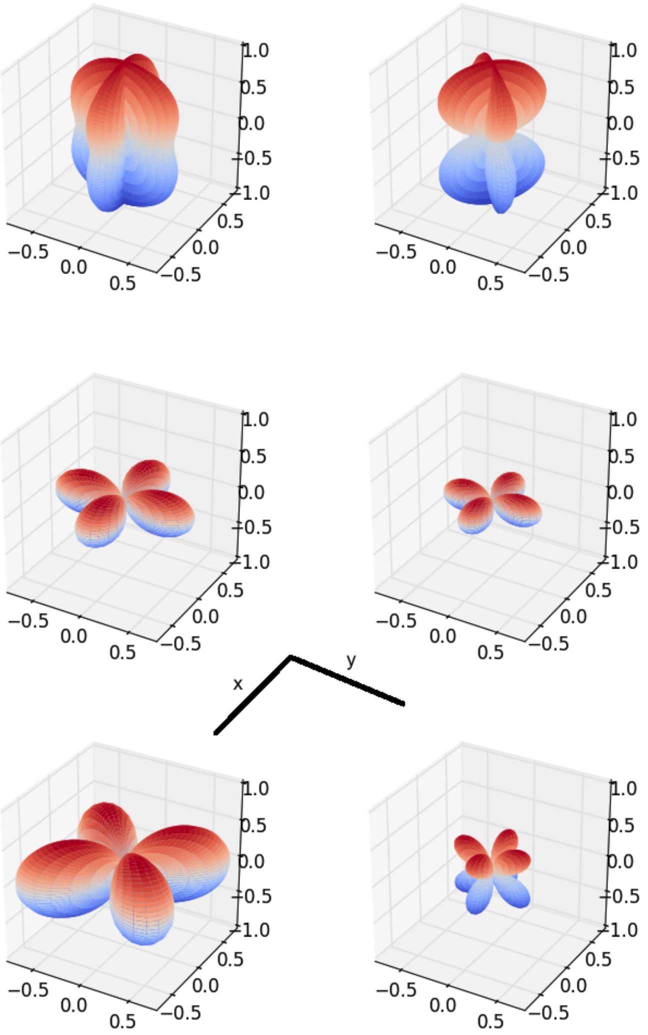

Figure 4: Antenna pattern functions, $|F_A(\hat{\mathbf{\Omega}})|$, for the plus, cross, longitudinal, breathing, y, and x modes from top to bottom. The axes are given by the interferometer schematic in the middle of the figure.

In the frequency domain the cross-correlation statistic, Y, is defined as

$$Y = \int_{-\infty}^{\infty} df \int_{\infty}^{\infty} df' \delta_T(f - f') \tilde{s}_I^*(f) \tilde{s}_J(f') \tilde{Q}(f'), \tag{15}$$

where $\delta_T(f)$ is the finite-time approximation for a delta function and $\tilde{Q}(f)$ is a filter function that can be chosen to maximize the signal-to-noise ratio. The ensemble average of Y is given by

$$\begin{aligned} \mu &\equiv \langle Y \rangle \qquad (16) \\ &= \int_{-\infty}^{\infty} df \int_{\infty}^{\infty} df' \delta_T(f - f') \langle \tilde{h}_I^*(f) \tilde{h}_J(f') \rangle \tilde{Q}(f'), \qquad (17) \end{aligned}$$

which can be written in terms of the energy density due to each polarization as

$$\mu = \frac{3H_0^2}{20\pi^2} T \int_{-\infty}^{\infty} df |f|^{-3} [\Omega_{gw}^T \gamma^T + \Omega_{gw}^V \gamma^V + \xi \Omega_{gw}^S \gamma^S] \tilde{Q}(f), \tag{18}$$

by substituting Eq. 14 into Eq. 19 [7]. The gravitational wave energy densities for each polarization are given by

$$\begin{aligned} \Omega_{gw}^T &= \Omega_{gw}^+ + \Omega_{gw}^\times, \qquad (19) \\ \Omega_{gw}^V &= \Omega_{gw}^x + \Omega_{gw}^y, \qquad (20) \\ \Omega_{gw}^S &= \Omega^b (1 + \kappa), \quad \kappa \equiv \Omega_{gw}^l / \Omega_{gw}^b. \qquad (21) \end{aligned}$$

In Eq. 18, the parameter ξ is given by $\frac{1}{3}(1 + 2\kappa)/(1 + \kappa)$ and represents the ratio of the energy densities of the longitudinal and breathing modes [7]. The overlap reduction functions γ, which describe the degree of correlation between signals in two detectors and depend on the detector geometry, will be discussed in the next section.

Using the weak signal assumption and Eq. 19, the variance of the correlation signal is

$$\begin{aligned} \sigma^2 &\equiv \langle Y^2 \rangle - \langle Y \rangle^2 \approx \langle Y^2 \rangle \qquad (22) \\ &\approx \frac{T}{4} \int_{-\infty}^{\infty} df P_I(|f|) P_J(|f|) |\tilde{Q}(f)|^2 \qquad (23) \end{aligned}$$

where $P_I(|f|)$ is the one-sided noise power spectrum density for detector I and T is the total observation time. The signal-to-noise ratio is defined as $\mathrm{SNR} \equiv \mu/\sigma$ so the filter function that maximizes this quantity is

$$\tilde{Q}(f) = K \frac{\gamma(f) \Omega_{gw}(|f|)}{|f|^3 P_I(|f|) P_J(|f|)}, \tag{24}$$

where $\Omega_{gw}^T \gamma^T + \Omega_{gw}^V \gamma^V + \xi \Omega_{gw}^S \gamma^S$ is abbreviated as $\gamma(f) \Omega_{gw}$ and K is some normalization constant [7].

2.3 Overlap Reduction Functions

For two coincident, coaligned detectors, $\gamma(f)$ is normalized to 1, but a separation between the detectors or lack of perfectly parallel arm alignment will result in a decrease in sensitivity. These two factors imply that there is only partial overlap between the gravitational strains recorded in the two detectors [1]. For each polarization and detector pair IJ, γ is defined as

$$\gamma^T_{IJ} \equiv \frac{5}{8\pi}\int_{S^2} e^{2\pi i f \hat{\mathbf{\Omega}}\cdot\Delta\vec{X}/c}(F^+_I F^+_J + F^\times_I F^\times_J)d\Omega, \tag{25}$$

$$\gamma^V_{IJ} \equiv \frac{5}{8\pi}\int_{S^2} e^{2\pi i f \hat{\mathbf{\Omega}}\cdot\Delta\vec{X}/c}(F^x_I F^x_J + F^y_I F^y_J)d\Omega, \tag{26}$$

$$\gamma^S_{IJ} \equiv \frac{5}{4\pi}\int_{S^2} e^{2\pi i f \hat{\mathbf{\Omega}}\cdot\Delta\vec{X}/c}(F^l_I F^l_J + F^b_I F^b_J)d\Omega. \tag{27}$$

Because γ depends only on the detector geometry, the expression for each polarization can be expanded analytically in terms of tensorial bases following the derivation in [1]:

$$\gamma^M_{IJ} = \rho^M_1(\alpha)D^{ij}_l D^J_{ij} + \rho^M_2(\alpha)D^i_{I,k}D^{kj}_J \hat{d}_i\hat{d}_j + \rho^M_3(\alpha)D^{ij}_I D^{kl}_J \hat{d}_i\hat{d}_j\hat{d}_k\hat{d}_l, \tag{28}$$

$$\alpha = \frac{2\pi f|\Delta\vec{X}|}{c}. \tag{29}$$

D_{ij} is the detector tensor defined in Section 2.1, $\Delta\vec{X}$ is the distance vector between the two detectors in the Earth-based coordinate system, and $\hat{d}_i$ is the unit vector in the direction of $\Delta\vec{X}$. The coefficients of Eq. 30 can be written in terms of the n$^{\text{th}}$ spherical bessel function of α as in [7]:

$$\begin{pmatrix}\rho^T_1\\ \rho^T_2\\ \rho^T_3\end{pmatrix} = \frac{1}{14}\begin{pmatrix}28 & -40 & 2\\ 0 & 120 & -20\\ 0 & 0 & 35\end{pmatrix}\begin{pmatrix}j_0\\ j_2\\ j_4\end{pmatrix},$$

$$\begin{pmatrix}\rho^V_1\\ \rho^V_2\\ \rho^V_3\end{pmatrix} = \frac{2}{7}\begin{pmatrix}7 & 5 & -2\\ 0 & -15 & 20\\ 0 & 0 & -35\end{pmatrix}\begin{pmatrix}j_0\\ j_2\\ j_4\end{pmatrix},$$

$$\begin{pmatrix}\rho^S_1\\ \rho^S_2\\ \rho^S_3\end{pmatrix} = \frac{1}{7}\begin{pmatrix}14 & 20 & 6\\ 0 & -60 & -60\\ 0 & 0 & 105\end{pmatrix}\begin{pmatrix}j_0\\ j_2\\ j_4\end{pmatrix}.$$

The overlap reduction functions calculated using both the numerical and analytical expressions are plotted in Figure 5. The apparent disagreement at high frequencies is due to sampling the numerical calculation on a logarithmic scale in frequency to minimize computation time. A comparison of overlap reduction functions for the three polarizations is shown in Figure 6.

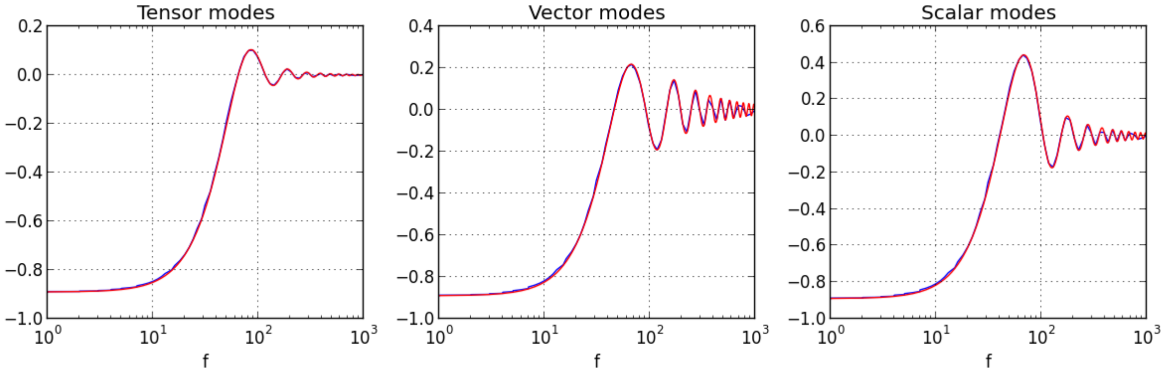

Figure 5: Overlap reduction function, γ as a function of frequency in Hz for the tensor, vector, and scalar modes calculated using the numerical integration over all space (blue) and using the analytical spherical bessel function expressions (red). The two methods are equivalent so the curves directly overlap in all three cases.

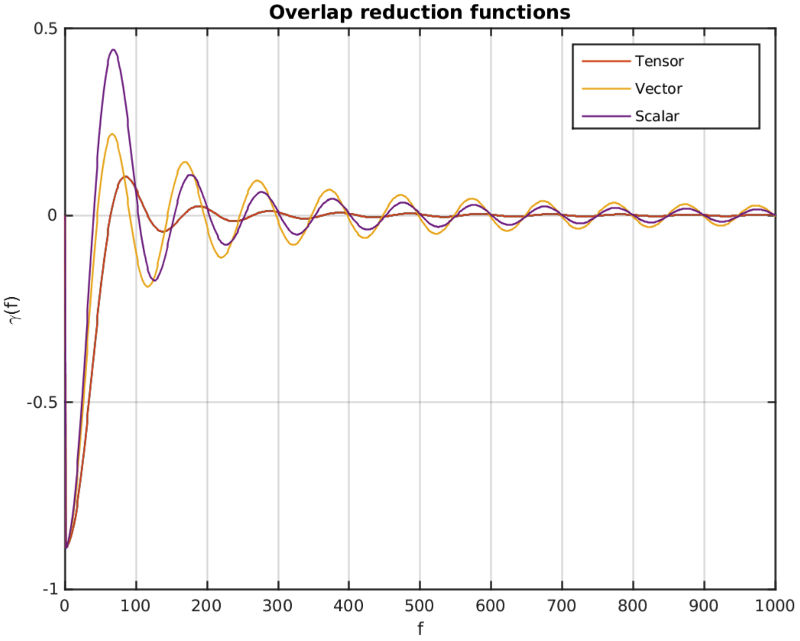

Figure 6: Comparison of the overlap reduction functions for the three polarizations as a function of frequency in Hz.

3 Simulations

3.1 Recovering Injected Gaussian Noise

In preparation for modifying the stochastic pipeline to search for a background from non-tensorial polarizations in real data, we ran the search over simulated Gaussian detector noise. After modifying the overlap reduction function script to include the vector and scalar polarizations, we used the predicted noise power spectrum density for aLIGO design sensitivity to inject detector noise for a period of 25,786 seconds starting on Oct 15 2015 14:29:43 UTC. For each of the three polarizations, $\sigma(f)$ was computed following the formalism outlined in the previous section, and the results are shown in Figure 7. The spikes in the distributions are caused by the zeros of the overlap reduction functions, and the tensor polarization appears to be the least sensitive at high frequencies.

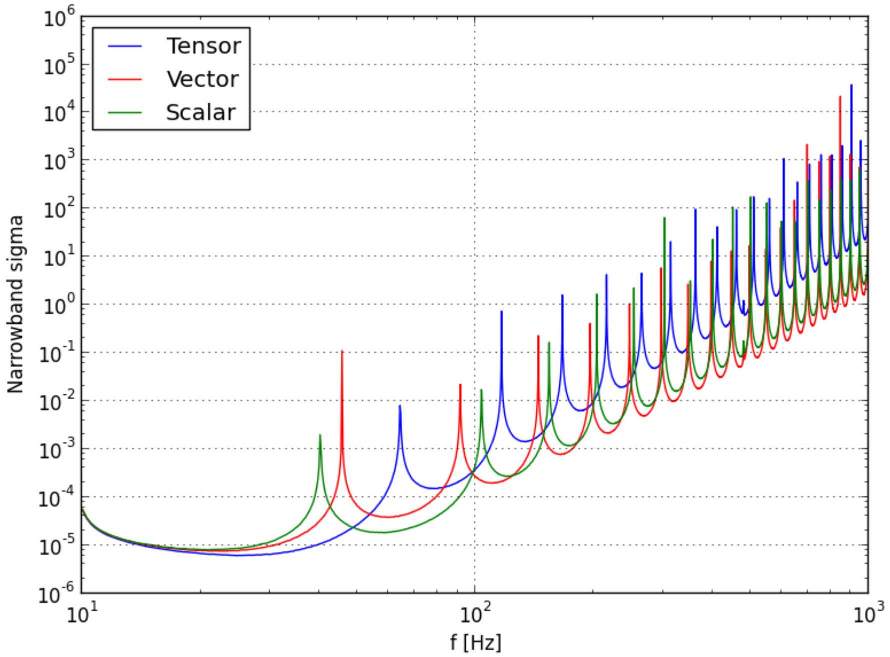

Figure 7: Detector sensitivity to Gaussian noise injected for 25,786 seconds on Oct 15 2015 14:29:43 UTC recovered using all three polarizations. The zeros of the overlap reduction functions cause the spikes in the $\sigma(f)$ distributions, and there appears to be a significant sensitivity difference between the tensor and non-tensorial polarizations at high frequencies.

3.2 Recovering a Simulated Signal

The next test of the modified pipeline was to verify its ability to recover a simulated signal. Tensor, vector, and scalar signals with amplitude $\Omega_{gw} = 2 \times 10^{-7}$ and spectral index $\alpha = 0$ were independently injected for the same time period as the simulated Gaussian noise. The simulated signal was then recovered assuming each polarization in turn as the model. The simulated strain for each detector for a given injected polarization, A, is given by

$$\tilde{h}_I^A(f) = \sqrt{\gamma_{II}^A(f)}\left(\sqrt{\frac{1+s(f)}{2}}z_1(f) + \frac{\gamma_{IJ}^A(f)}{\sqrt{2\gamma_{II}^A(f)\gamma_{JJ}^A(f)(1+s(f))}}z_2(f)\right), \tag{30}$$

$$\tilde{h}_J^A(f) = \sqrt{\gamma_{JJ}^A(f)}\left(\sqrt{\frac{1+s(f)}{2}}z_2(f) + \frac{\gamma_{IJ}^A(f)}{\sqrt{2\gamma_{II}^A(f)\gamma_{JJ}^A(f)(1+s(f))}}z_1(f)\right), \tag{31}$$

where

$$s(f) = \sqrt{\frac{1-(\gamma_{IJ}^A(f))^2}{\gamma_{II}^A(f)\gamma_{JJ}^A(f)}}. \tag{32}$$

The functions $z_1(f)$ and $z_2(f)$ are complex numbers whose real and imaginary parts are drawn randomly from the standard normal distribution for each frequency and then normalized by a factor of $\sqrt{\frac{3NH_0^2}{20\Delta T\pi^2}}$, where N is the number of samples and ΔT is the inverse of the resample rate. The factors of γ in Eqs. 32 and 33 are chosen such that $\langle(\tilde{h}_I^A(f))^*\tilde{h}_J^A(f)\rangle = \frac{1}{2}S^A(f)\gamma_{IJ}^A(f)$. The procedure for recovering the signal remains the same as was detailed in Section 2.2, but the optimal filter, $\tilde{Q}(f)$, now becomes

$$\tilde{Q}(f) = K\frac{\gamma_{IJ}^M(f)\Omega_{gw}^M(|f|)}{|f|^3P_I(|f|)P_J(|f|)}, \tag{33}$$

where M is the polarization assumed on recovery.

Figure 8 shows the narrowband point estimate, $Y(f)$, and sensitivity, $\sigma(f)$ for injected tensor, vector, and scalar signals, respectively. The blue curves indicate recovery assuming a tensor model, the red indicates a vector model, and the green a scalar model. The point estimate is normalized such that $\langle Y(f)\rangle = \Omega_{gw}(f)$, and the result is consistent with the injected signal of $\Omega_{gw}(f) = 2\times10^{-7}$ at low frequencies where the stochastic search is most sensitive. Similar to the case of simulated Gaussian noise, the tensor mode is less sensitive than the vector and scalar modes at high frequencies.

The broadband point estimates and sensitivities are shown in Figures 9, 10, and 11, along with the segment-by-segment SNR and the cumulative SNR as a function of total observation time. The cumulative values, summed over the observation times i, are given by:

$$Y = \frac{\sum Y_i \sigma_i^{-2}}{\sum \sigma_i^{-2}}, \qquad \sigma^{-2} = \sum \sigma_i^{-2}, \qquad \mathrm{SNR} = \sqrt{\frac{Y^2}{\sigma^2}}. \tag{34}$$

The cumulative sensitivities overlap for the vector and scalar modes, and the cumulative SNR is highest when the model chosen for recovery matches the injected polarization.

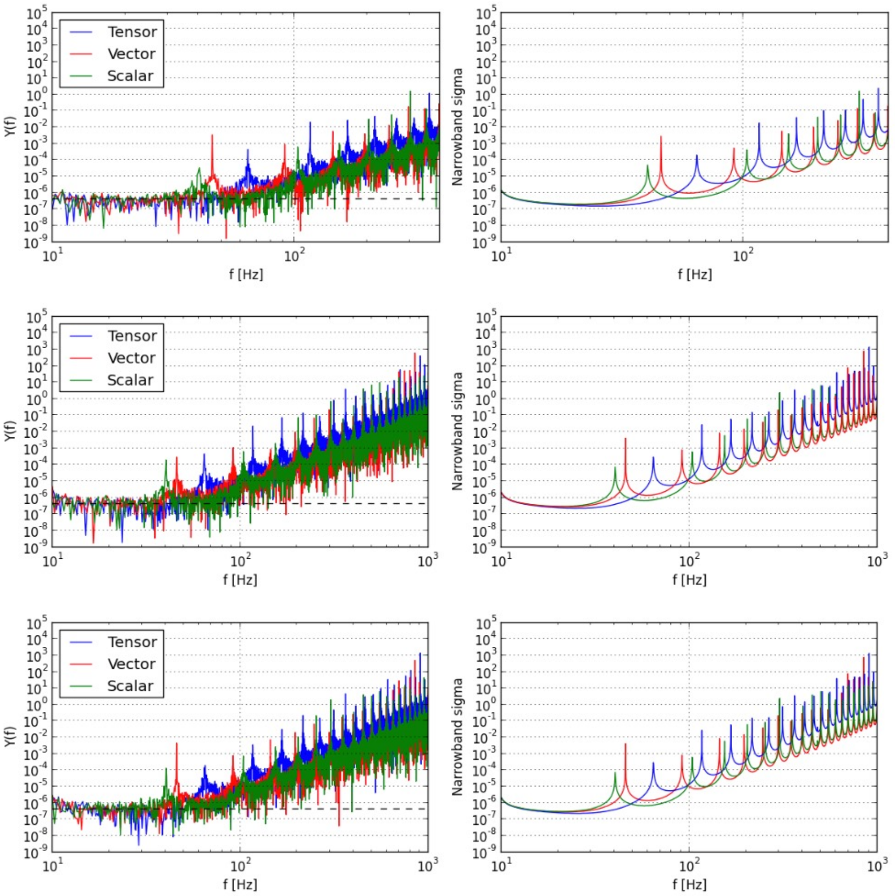

Figure 8: Narrowband point estimate and sensitivity for an injected tensor (top), vector (middle), and scalar (bottom) signal with $\Omega_{gw}(f) = 2 \times 10^{-7}$ recovered assuming tensor (blue), vector (red) and scalar (green) models independently. The dashed black line shows the expected signal. The peaks in both distributions are due to the zeros of the overlap reduction functions.

4 O1 Search

After verifying the validity of the single-polarization search with simulations, the aLIGO O1 data was analyzed using the same analysis methods. The data was divided into half-overlapping 192 sec intervals and down sampled to 4096 Hz. A Hann window and high-pass filter are applied to each segment, and the data is then coarse-grained to a frequency of 1/32 Hz. The data used in this analysis was selected such that both detectors were in low-noise science mode, so certain segments were cut based on known non-stationarity effects. The total observation time after applying these cuts is 28.5 days. Data quality cuts are also applied in the frequency domain for frequencies with large noise power spectra usually due to instrumental effects [16]. As a further test of the modified search pipeline, the analysis was run for a tensor signal, and the results matched those of the official LIGO stochastic isotropic search to within a few percent. This minor discrepancy is likely due to slight differences in the methods used to combine broadband σ while post-processing the data. Finally, before running the unblinded search for vector and scalar modes, we ran this same search but introduced a 1 sec time shift in one of the detector data streams, effectively removing any potential correlations of astrophysical origin, but maintaining instrumental correlations.

The unblinded scalar results are shown in Figures 12 and 14, and the vector results in Figures 13 and 15. [redacted]

5 Model Selection

5.1 Signal to Noise Ratio

While the above analysis allowed us to search for a signal of a single polarization, generic backgrounds may be composed of multiple polarizations simultaneously. The definitions of the point estimate and the sensitivity must be adjusted for such a mixed-polarization signal. Converting the integrals in Equations 20 and 25 to sums over frequency gives

$$\mu = \frac{3H_0^2}{10\pi^2} T \sum \frac{\gamma(f)\Omega_{gw}(f)\tilde{Q}(f)}{f^3} df, \tag{35}$$

$$\sigma^2 = \frac{T}{2} \sum \tilde{Q}^2(f) P_1(f) P_2(f) df, \tag{36}$$

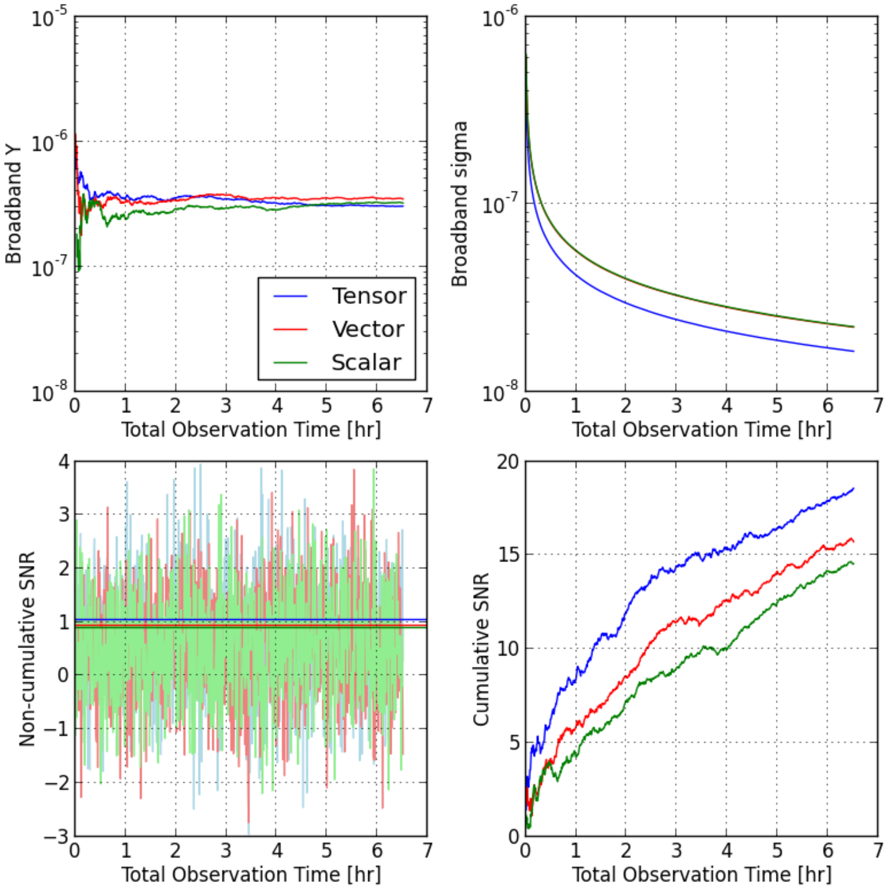

Figure 9: Cumulative broadband point estimate and sensitivity as a function of total observation time for an injected tensor signal with $\Omega_{gw}(f) = 2 \times 10^{-7}$ recovered assuming tensor (blue), vector (red) and scalar (green) models independently. The vector and scalar sensitivities overlap. While the point estimate is highest for recovery with the vector model, both the segment-by-segement and cumulative SNRs are greater when recovering the signal with the tensor polarization. The mean segment-by-segment SNR is given by the horizontal lines for each polarization in the lower left plot.

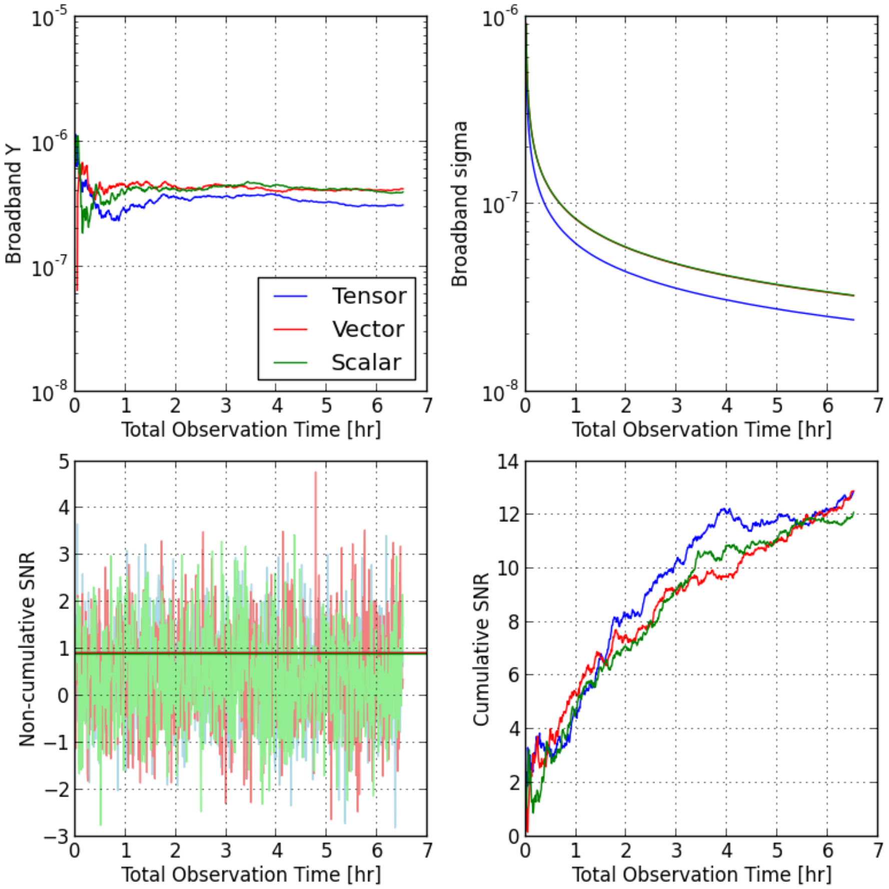

Figure 10: Cumulative broadband point estimate and sensitivity as a function of total observation time for an injected vector signal with $\Omega_{gw}(f) = 2 \times 10^{-7}$ recovered assuming tensor (blue), vector (red) and scalar (green) models independently. The vector and scalar sensitivities overlap, while the cumulative SNR assuming a vector model on recovery exceeds that of the tensor model only at the end of the observing period.

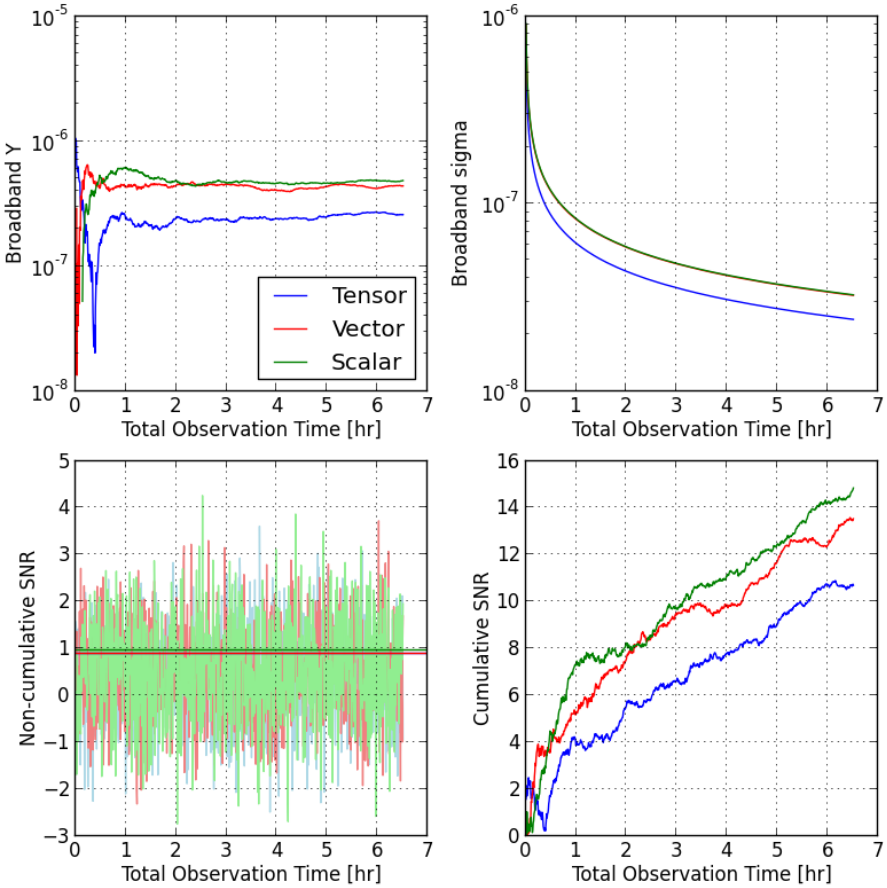

Figure 11: Cumulative broadband point estimate and sensitivity as a function of total observation time for an injected scalar signal with $\Omega_{gw}(f) = 2 \times 10^{-7}$ recovered assuming tensor (blue), vector (red) and scalar (green) models independently. The sensitivities and average segment-by-segment SNR overlap for the vector and scalar recovery models.

[redacted]

[redacted]

[redacted]

[redacted]

where we have multiplied by a factor of 2 to account for summing only over positive frequencies, and we have again taken $\gamma(f)\Omega_{gw}$ to include all polarizations:

$$\gamma(f)\Omega_{gw} = \Omega^T_{gw}\gamma^T + \Omega^V_{gw}\gamma^V + \xi\Omega^S_{gw}\gamma^S. \tag{37}$$

The broadband values μ and σ are computed from the narrowband values $Y(f)$ and $\sigma(f)$ following

$$\mu = \frac{\sum Y(f)\sigma^{-2}(f)}{\sum \sigma^{-2}(f)}, \qquad \sigma^{-2} = \sum \sigma^{-2}(f), \tag{38}$$

so the expression for SNR^2 is equivalently given by

$$\text{SNR}^2 = \frac{\mu^2}{\sigma^2} = \frac{\left[\frac{3H_0^2}{10\pi^2} T \sum \frac{\gamma(f)\Omega_{gw}(f)\tilde{Q}(f)}{f^3} df\right]^2}{\frac{T}{2}\sum \tilde{Q}^2(f)P_1(f)P_2(f)df}, \tag{39}$$

and

$$\text{SNR}^2 = \left[\frac{\sum Y(f)\sigma^{-2}(f)}{\sum \sigma^{-2}(f)}\right]^2 \sum \sigma^{-2}(f) = \frac{\left[\sum Y(f)\sigma^{-2}(f)\right]^2}{\sigma^{-2}(f)}. \tag{40}$$

Setting the numerators and denominators of Equations 41 and 42 equal to each other and then solving for $\tilde{Q}(f)$ such that $Y(f) = \gamma(f)\Omega_{gw}(f)$ gives

$$\tilde{Q}(f) = \left(\frac{3H_0^2}{10\pi^2}\right)\frac{2}{f^3 P_1(f)P_2(f)}. \tag{41}$$

The expression for SNR^2 then simplifies to

$$\text{SNR}^2 = \left(\frac{3H_0^2}{10\pi^2}\right)^2 2T \frac{\left[\sum \frac{\gamma(f)\Omega_{gw}(f)}{f^6 P_1(f)P_2(f)} df\right]^2}{\sum \frac{1}{f^6 P_1(f)P_2(f)df}}. \tag{42}$$

However, since the background is not necessarily flat in each frequency bin, the signal must be weighted by the model assumed on recovery, $\gamma_M(f)\Omega_M(f)$, which is also a sum of the overlap reduction functions and contributions from each polarization as in Equation 39 [14]. The expression for SNR^2 is now

$$\text{SNR}^2 = \left(\frac{3H_0^2}{10\pi^2}\right)^2 2T \frac{\left[\sum \frac{\gamma(f)\Omega_{gw}(f)\gamma_M(f)\Omega_M(f)}{f^6 P_1(f)P_2(f)} df\right]^2}{\sum \frac{(\gamma_M(f)\Omega_M(f))^2}{f^6 P_1(f)P_2(f)df}} \tag{43}$$

which simplifies to the expression for the optimal SNR when the model matches the signal, $\gamma_M(f)\Omega_M(f) = \gamma(f)\Omega_{gw}(f)$:

$$\text{SNR}^2 = \left(\frac{3H_0^2}{10\pi^2}\right)^2 2T \sum \frac{(\gamma(f)\Omega_{gw}(f))^2}{f^6 P_1(f)P_2(f)}. \tag{44}$$

	Recover Tensor	Recover Vector	Recover Scalar
Inject	18.56	15.72	14.55
Tensor	18.90	16.76	14.00
Inject	12.88	12.89	12.10
Vector	12.58	14.19	13.73
Inject	10.70	13.53	14.84
Scalar	10.30	13.5	13.91

Table 1: Predicted (top) and calculated (bottom) SNR values for the signals injected in Section 3.2. The horizontal axis indicates the model assumed when recovering the signal, while the vertical axis indicates the type of signal that was injected. The SNR is highest for both the prediction and the calculation when the model and the injected signal match, as indicated by the optimal SNR expression in Equation 46.

The SNR values predicted using Equation 45 for the signals injected in Section 3.2 are given in Table 1 in comparison to the values calculated from the data (following Equation 36). As indicated by the optimal SNR expression above, the maximum SNR for both the prediction and the calculation occurs when the injected signal and model match.

5.2 Component Separation

Using different models to maximize the SNR defined in the last section is one way to determine contributions from individual polarizations to a recorded signal. The same component separation goal can also be achieved using the Fisher information matrix for a system with at least three detectors (unlike aLIGO). For a given detector pair β, we define the following quantities:

$$Y_\beta(f) \equiv \frac{2}{T}\tilde{s}^*_{\beta_1}(f)\tilde{s}_{\beta_2}(f), \tag{45}$$

$$\mathcal{N}_{\beta\beta'}(f,f') \equiv \langle Y^*_{\beta'}(f')Y_\beta(f)\rangle - \langle Y^*_{\beta'}(f')\rangle\langle Y_\beta(f)\rangle. \tag{46}$$

$Y_\beta(f)$ is the cross-correlation statistic for the baseline β and $\mathcal{N}_{\beta\beta'}(f,f')$ is a diagonal matrix whose elements are the products of the noise power spectrum densities of the two detectors in the given baseline. The likelihood function for the data Y given a model $\mathcal{A}$ is a Gaussian assuming that the noise itself is Gaussian, much louder than the signal, and uncorrelated between the two detectors [15]:

$$p(Y|\mathcal{A}) \propto \exp\big[-\frac{1}{2}(Y - M\mathcal{A})^T\mathcal{N}^{-1}(Y - M\mathcal{A})\big] \tag{47}$$

where the matrices M and $\mathcal{A}$ are given by

$$M = \begin{pmatrix} \gamma_1^T & \gamma_1^V & \gamma_1^S \\ \gamma_2^T & \gamma_2^V & \gamma_2^S \\ \vdots & \vdots & \vdots \\ \gamma_N^T & \gamma_N^V & \gamma_N^S \end{pmatrix}, \qquad \mathcal{A} = \begin{pmatrix} \Omega^T(f) \\ \Omega^V(f) \\ \Omega^S(f) \end{pmatrix},$$

for $\beta = 1, 2, \cdots, N$ and where γ_β^A is the overlap reduction function for the polarization A for the detector pair β. The background amplitudes maximizing the likelihood are

$$\mathcal{A} = F^{-1}X, \tag{48}$$

where

$$F \equiv M^T \mathcal{N}^{-1} M, \qquad X \equiv M^T \mathcal{N}^{-1} Y. \tag{49}$$

F is the Fisher information matrix, whose inverse is the covariance matrix for $\mathcal{A}$ in the large-SNR limit:

$$F^{-1} \approx \langle \mathcal{A}\mathcal{A}^T \rangle - \langle \mathcal{A} \rangle \langle \mathcal{A}^T \rangle. \tag{50}$$

This separation procedure can only be applied to a system with at least three detector pairs, but it can be modified for a single detector baseline. The matrices M and $\mathcal{A}$ become

$$M = \begin{pmatrix} \gamma^T(f_1)\left(\frac{f_1}{f_0}\right)^\alpha & \gamma^V(f_1)\left(\frac{f_1}{f_0}\right)^\alpha & \gamma^S(f_1)\left(\frac{f_1}{f_0}\right)^\alpha \\ \gamma^T(f_2)\left(\frac{f_2}{f_0}\right)^\alpha & \gamma^V(f_2)\left(\frac{f_2}{f_0}\right)^\alpha & \gamma^S(f_2)\left(\frac{f_2}{f_0}\right)^\alpha \\ \vdots & \vdots & \vdots \\ \gamma^T(f_N)\left(\frac{f_N}{f_0}\right)^\alpha & \gamma^V(f_N)\left(\frac{f_N}{f_0}\right)^\alpha & \gamma^S(f_N)\left(\frac{f_N}{f_0}\right)^\alpha \end{pmatrix}, \qquad \mathcal{A} = \begin{pmatrix} \Omega^T \\ \Omega^V \\ \Omega^S \end{pmatrix},$$

where the spectral index α is fixed for some reference frequency f_0 and $\mathcal{A}$ represents just the amplitudes of the different polarizations [14]. Equation 43 can then be used to solve for $\mathcal{A}$ as above.

5.3 Conclusion and Outlook

[redacted] The long term goal is to then construct a component separation scheme for the current aLIGO two-detector system and for the three detector system including the Virgo detector, [redacted]

Special thanks to the National Science Foundation for sponsoring this REU program. Thank you also to Dr. Alan Weinstein and the LIGO Collaboration for giving me the opportunity to participate in this program and to the Caltech SFP Office for organizing it. This work would not have been possible without the incredible guidance of my mentor, Tom Callister. Finally, thank you to my fellow LIGO SURF students for the moral support and for ensuring that I have a wonderful experience.

References

[1] B. Allen and J.D. Romano, Phys. Rev. D **59**, 102001 (1999).
[2] T. Regimbau and V. Mandic, Class. Quantum Grav. **25**, 184018 (2008).
[3] E. Thrane and J.D. Romano, Phys. Rev. D **88**, (2013).
[4] J. Aasi et al. (LIGO and Virgo Collaboration) Phys. Rev. Lett. **113**, 231101 (2014).
[5] R.D. Branford and K.S. Thorne, *Random Processes*, (version 1206.1.K, 2012), pp.1-37.
[6] B.S. Sathyaprakash and B.F. Schutz, Living Rev Relativity **12**, 2 (2009).
[7] A. Nishizawa et al. Phys. Rev. D **79**, 082002 (2009).
[8] P.R. Saulson, Am. J. Phys. **65**, 501 (1997).
[9] *An Introduction to LIGO and Gravitational Waves*, http://www.ligo.org/science.php
[10] *A Comprehensive Overview of Advanced LIGO*, https://www.advancedligo.mit.edu/summary.html
[11] *LIGO Does It Again: A Second Robust Binary Black Hole Coalescence Observed* https://www.ligo.caltech.edu/news/ligo20160615
[12] A. Nishizawa and K. Hayama, Phys. Rev. D **88**, 064005 (2013).
[13] B.F. Schutz, Am. J. Phys. **52**, 412 (1984).
[14] Correspondence with Tom Callister.
[15] Correspondence with Joe Romano.
[16] B.P. Abbott et al. (LIGO and Virgo Collaboration) *In Progress.*